MATERIALS SCIENCE

Inverse design of guanine-defects in carbon nanotubes for high-resolution emission tuning

Yinong Li[1], Xiao-Kun Zhao[2], Jiajie Wu[1], Li Zhu[1], Shishan Tian[1], Yannan Feng[1], Zhilong Zhang[1], Cong-Qiao Xu[2], Zhiwei Lin[1,3]*

Defect engineering in single-wall carbon nanotubes (CNTs) offers a powerful means of tuning their properties. However, existing strategies predominantly rely on post hoc characterization of defects, and rational approaches for the pre-design of defects remain lacking. Here, we present an inverse defect-design strategy that leverages DNA-directed, guanine-specific chemistry to introduce guanine-defects into CNTs. We assign these modifications as sp^2 defects, which—unlike conventional sp^3 defects—largely preserve the π-conjugation of CNT lattice while enabling tunable property modulation via lattice restructuring. This approach was applied to five distinct single-chirality CNT species, yielding a chirality-dependent modification index, M(*n*, *m*), capable of predicting defect-induced property changes, even for CNTs lacking prior experimental data. Guided by this index, we achieved deterministic control over emission wavelengths with an accuracy of ±1 nm and Raman profiles within 1% deviation from predictions. These precisely engineered CNTs were further utilized for pattern switching and multilayer information encryption, highlighting the potential of precision defect design in advancing next-generation CNT-based materials.

INTRODUCTION

In crystalline materials, many of the most fascinating properties arise not from the perfect lattice, but from the defects within. A prime example is doped crystalline silicon, where the deliberate introduction of defects transforms an intrinsic semiconductor into either N-type or P-type, enabling precise control over its electronic properties (*1*–*3*). Single-wall carbon nanotubes (CNTs), with their exceptional electrical and optical properties, present an especially compelling platform for defect engineering (*4*–*8*). Unlike bulk crystals, the entire lattice of CNTs is exposed at the surface, rendering them highly amenable to chemical modification. Extensive efforts have demonstrated that introducing defects by chemical modification can profoundly alter CNT properties (*9*–*21*). Oxygen doping, for instance, modulates near-infrared band gaps (*9*, *12*, *20*, *21*), while low-density quantum defects markedly enhance photoluminescence (*10*, *11*, *13*). These defect-modified CNTs have facilitated encouraging applications ranging from single-photon emission to cancer diagnosis (*12*, *14*, *22*, *23*).

Despite these advances, chemical modifications of CNTs have so far depended entirely on post hoc analysis (Fig. 1A, left), and an effective strategy for pre-designing defects to confer specific, targeted CNT properties remains lacking. The key challenges are twofold: (i) how to effectively integrate the intrinsic electronic structures of CNTs with defects, as most chemical reactions introduce sp^3 defects into the sp^2 lattice of CNTs (*10*, *13*–*15*, *24*, *25*). The resulting properties of modified CNTs are governed by the combined effects of both the disruption of lattice structures and the chemical nature of functional groups (*10*, *14*, *26*, *27*); and (ii) how to establish a generalized principle for predicting the impact of defects across various CNTs chiralities, as each chirality type of CNT exhibits distinct sensitivity to defects.

In this work, we introduce an inverse defect design strategy that allows for the precise functionalization of CNTs with predetermined optical properties (Fig. 1A, right). Our approach modifies CNTs through a DNA-directed, guanine (G)-specific chemistry (*28*–*32*). While our previous work demonstrated the feasibility of using this chemistry for spatially ordered G-functionalization on (8,3) CNTs (*16*), the underlying nature of these modifications and the physical principles governing their optical response across different CNT chiralities remained elusive. In the present study, we move beyond phenomenological observations to establish a predictive framework for defect engineering.

By combining systematic experiments with theoretical calculations, we elucidate the fundamental mechanisms by which these guanine-defects modify the CNT lattices and regulate their properties. Critically, we demonstrate that these modifications effectively preserve the π-conjugated system of the nanotubes, leading us to assign them as sp^2 defects. This nature is intrinsically distinct from the extensively studied sp^3 defects, which typically disrupt the lattice conjugation. Our results show that the properties of the functionalized CNTs are predominantly determined by defect-induced lattice restructuring rather than covalent disruption. The modification of five distinct types of single-chirality CNTs has revealed a quantitative framework, defined by a modification index M(*n*, *m*), that guides precise defect design. This framework enables the tailorable modification of CNTs, yielding emission wavelengths accurate to within ±1 nm and Raman profiles that align within 1% of theoretical models. Finally, we showcase the application of sp^2 defect-modified CNTs with customized optical properties in pattern switching and multilayer information encryption.

RESULTS

Construction of guanine-defects in CNTs

This study employs high-purity single-chirality CNTs for chemical modification, allowing for an unambiguous assessment of the impact of defects on the structure and properties of functionalized tubes. Six distinct types of chirality-pure CNTs were separated using

[1]South China Advanced Institute for Soft Matter Science and Technology, State Key Laboratory of Luminescent Materials and Devices, School of Emergent Soft Matter, South China University of Technology, Guangzhou 510640, China. [2]Department of Chemistry, Guangdong Provincial Key Laboratory of Catalytic Chemistry, Southern University of Science and Technology, Shenzhen 518055, China. [3]Guangdong Provincial Key Laboratory of Functional and Intelligent Hybrid Materials and Devices, Guangdong Basic Research Center of Excellence for Energy and Information Polymer Materials, South China University of Technology, Guangzhou 510640, China.
*Corresponding author. Email: zhiweilin@scut.edu.cn

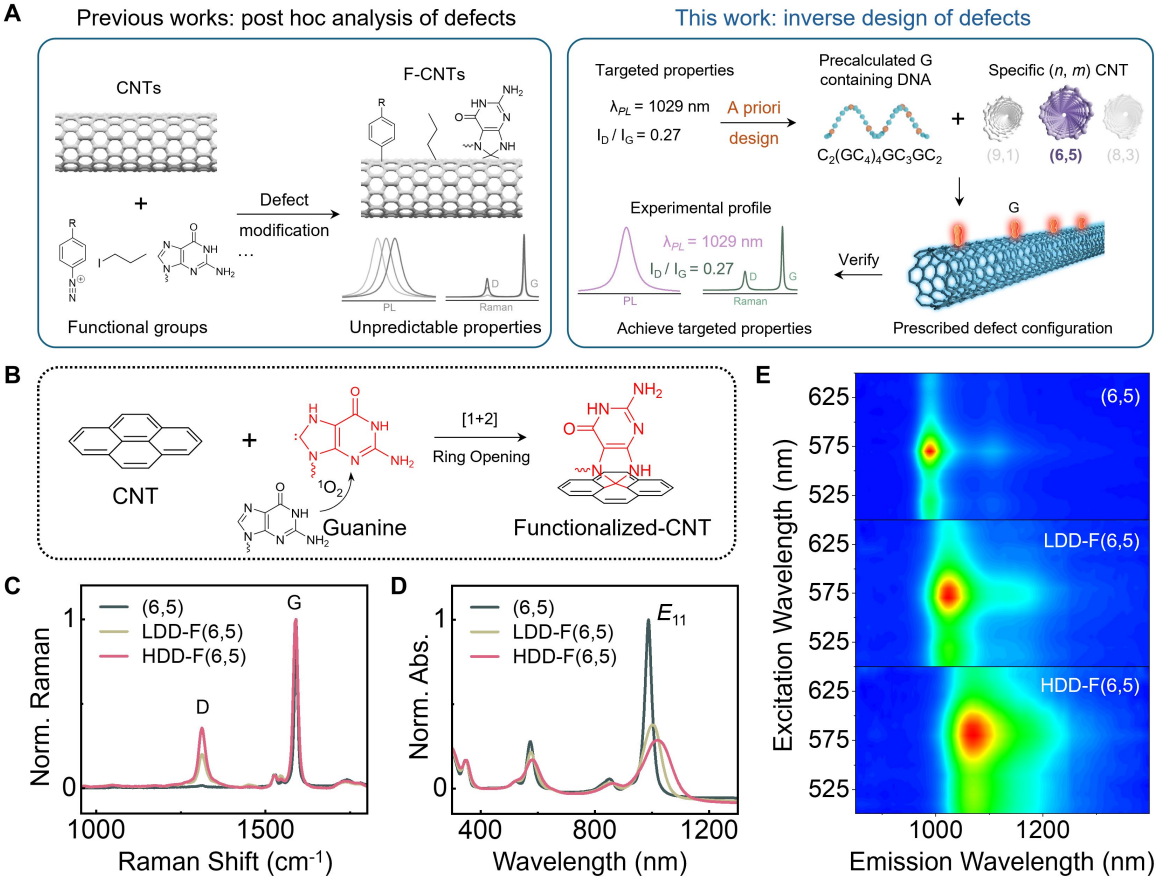

Fig. 1. Design and construction of guanine-defects in CNTs. (**A**) Comparison of conventional and inverse-design strategies for CNT defect engineering. Conventional approaches (left) typically rely on the post hoc characterization of stochastic modifications, where the resulting properties of F-CNTs are unpredictable prior to reaction. In contrast, this work introduces an inverse-design strategy (right) that enables the a priori calculation and implementation of specific defect configurations. This deterministic approach allows for the precise engineering of targeted, high-resolution optical properties of F-CNTs. (**B**) Illustration of the reaction between CNTs and guanine to introduce sp^2 defects (see more details in fig. S2). (**C**) Raman spectra of F(6,5) with varying defect densities, where the D-peaks enhance as defect density rises. (**D**) Absorption spectra and (**E**) 2D excitation-emission spectra of F(6,5) with different defect densities. The intensities were normalized to clearly visualize the defect-induced emission peaks. LDD-F(6,5) and HDD-F(6,5) were modified with 30-mer DNA oligonucleotides containing 5G and 10G, $C_3(GC_5)_4GC_2$ and $C(GCC)_9GC$, respectively. LDD, low defect density; HDD, high defect density.

a DNA-based protocol through an aqueous two-phase system (*33*–*36*) (fig. S1). We first introduced defects into the (6,5) species using the one-pot guanine chemistry (Fig. 1B and fig. S2), adapted from our previous work (*16*) (see figs. S3 to S5 and Materials and Methods for details). The defect densities in the functionalized (6,5) nanotubes (denoted as F(6,5)) can be modulated by altering the guanine (G) content in the reactive DNA sequences. We first analyzed two F(6,5) samples with low and high defect densities, labeled as LDD-F(6,5) and HDD-F(6,5), which were modified using 30-mer DNA oligonucleotides containing 5G and 10G, $C_3(GC_5)_4GC_2$ and $C(GCC)_9GC$, respectively.

Raman spectroscopy provides direct evidence of defect incorporation in CNTs (*17*). The D band, arising from defect-induced double-resonance phonon scattering (*37*), exhibits a pronounced increase in intensity relative to the G band upon functionalization (Fig. 1C). The normalized D intensity (I_D, normalized to the G band) was measured to be 0.212 for LDD-F(6,5) and 0.357 for HDD-F(6,5), consistent with the increased defect density. X-ray photoelectron spectroscopy (XPS) was employed to quantify the defect density of these modified CNTs. By analyzing the N/C atomic percentage ratio, the defect density of HDD-F(6,5) was estimated to be 3.6 ± 0.3 defects per nanometer (see fig. S6 for detailed analysis). For nanotubes with comparable I_D values, the defect density in these G-functionalized CNTs is 1–2 orders of magnitude higher than that in sp^3-defect modified nanotubes, which is approximately one defect per 20 nanometer (*10*). This disparity can be attributed to the sp^2 nature of G-induced defects, which causes minimal disruption to the sp^2 lattice and π-conjugation system of the nanotube framework (*38*–*40*), in contrast to sp^3 defects (*41*). This notion is further supported by density functional theory (DFT) calculation, as discussed in the following section.

The observed Raman spectral variations induced by guanine-defects align well with several previous studies on sp^2 defects. For instance, a comparative study of sp^2 and sp^3 defects demonstrated that while sp^2 defects generate a D-band, it is typically weaker than the band associated with sp^3 defects (*39*). Furthermore, studies on carbene/nitrene-based sp^2-defect modifications showed that such functionalization leads to D-band enhancement and subtle perturbations in the electronic structure of CNTs (*42*–*44*). While some

literature reported negligible D-band enhancement from sp^2 defects (*38*), this discrepancy may stem from lower defect densities (fig. S7) or the use of CNTs with reduced bond curvature. As discussed later, these defect-induced spectral variations are highly sensitive to CNT chirality.

UV-Vis-NIR absorption and photoluminescence (PL) spectra were used to further investigate the modified nanotubes (Fig. 1, D and E). The absorption spectrum shows a broadening and red-shifting of the E_{11} excitonic transition peak compared to the pristine (6,5) nanotubes. Despite the spectral broadening, the integrated absorbance intensity of the E_{11} transition remained virtually constant after modification (see additional discussion in fig. S8), indicating that the fundamental optical transitions of the nanotube framework in F(6,5) are preserved, rather than quenched or blocked. In contrast, previous studies on sp^3 defects-modified CNTs reported a dramatic decrease in absorption (*10*), which was attributed to the disruption of the extended π-network in CNTs (*40*, *41*, *45*, *46*).

The excitation-emission maps (Fig. 1E) and the corresponding 1D PL spectra (fig. S9) exhibit a unimodal, red-shifting E_{11} emission peak upon functionalization. The observed red shift in the E_{11} wavelength positively correlates with defect density. These observations are distinguished from sp^3-induced defects, which typically produce an additional E_{11}^- emission peak in CNTs (*9*, *10*, *47*), with the wavelength of both E_{11} and E_{11}^- remaining unaffected by defect density (*10*, *26*, *48*). While recent theoretical simulations suggested that G-functionalization may induce sp^3 defects on adjacent carbon sites (*32*), such configurations are characteristically associated with deep-trap emission features (E_{11}^-) (*49*, *50*). In our system, we observed a continuous redshift of the primary E_{11} rather than the emergence of a discrete E_{11}^- state. The absence of these deep-trap features signifies that these DNA-guided defects do not function as localized sp^3 traps, but rather induce a more delocalized sp^2 modification of the nanotube's π-system.

To facilitate a rigorous quantitative comparison with sp^3 defects, we specifically functionalized (6,5) CNTs using a $C_{15}GC_{15}$ DNA sequence (31-mer). This ensures a defect density identical to that reported in a recent study (*24*), which employed iodine-bearing 31-mer DNA to introduce sp^3 defects. In that study, the sp^3-defect modified CNTs exhibited a distinct, dramatically redshifted emission peak (E_{11}^-) at 1168 nm (a 178 nm shift), and a robust Raman I_D/I_G ratio of 0.157. In stark contrast, our G-functionalized CNTs display only a minimal 5 nm redshift in PL spectrum, and a remarkably low I_D/I_G ratio of 0.037 (fig. S7). Furthermore, the characteristic E_{11}^- peak of sp^3 defects was entirely absent in our samples. These results provide definitive evidence that the G-modified defects are fundamentally distinct from typical sp^3 defects, further validating their sp^2 nature.

Understanding guanine-defects by DFT and TA studies

To understand why guanine-defects impose distinct effects on the structures and properties of CNTs compared to sp^3 defects, we conducted a DFT analysis on the G-modified nanotubes. The LDD and HDD scenarios were modeled by attaching one and two hydrogen-capped guanine molecules to the sidewall of a hydrogen-capped (6,5) segment with one unit cell (fig. S10). For pristine (6,5), the energies of the highest occupied molecular orbital (HOMO) and the lowest unoccupied molecular orbital (LUMO) were calculated to be −4.657 eV and − 3.597 eV, respectively, resulting in a CNT-HOMO-LUMO gap of 1.060 eV (Fig. 2A). Upon functionalization, a minor change in the LUMO energy was observed: −3.572 eV for LDD-F(6,5) and − 3.561 eV for HDD-F(6,5), respectively. However, the HOMO energies exhibited more substantial variations, with the values of −4.068 eV and − 4.028 eV (Fig. 2A, grey energy levels). Further analysis revealed that these new HOMOs originate from the guanine groups rather than CNTs (fig. S11 and additional discussion). The electronic density of these orbitals is largely localized on the guanines, with minimal overlap with the π-conjugated system of the CNT framework. This signifies that the guanine-localized orbitals do not predominately dictate the electronic properties of the G-modified CNTs. We thus analyzed the HOMO-1 levels of LDD-F(6,5) and HDD-F(6,5), which correspond to the nanotube framework in modified CNTs. Their values are −4.622 eV for LDD-F(6,5) and −4.585 eV for HDD-F(6,5), yielding CNT-HOMO-LUMO gaps of 1.049 eV and 1.024 eV (Fig. 2A), respectively. The reduction in these gaps from pristine (6,5) to LDD-F(6,5) and then to HDD-F(6,5) aligns well with the observed red-shift in absorption spectra (Fig. 1D). Based on the changes of CNT-HOMO-LUMO gaps, we schematically outlined the density of states of CNTs (Fig. 2B), where Abs and Abs* denote the absorption of pristine and modified CNTs, respectively. Compared with Abs, the reduced E_{11} transition gap in Abs* accounts for the observed red shift (a more detailed discussion follows in subsequent paragraphs).

The results above indicate that the electronic properties of G-modified CNTs are primarily governed by the defect-induced lattice structure changes, rather than by the guanine functional groups. To further validate this hypothesis, we replaced guanine with a -CH_2 group (Fig. 2A and fig. S12) and calculated the CNT-HOMO-LUMO gap for this CH_2-F(6,5) model. The calculated gap was 1.045 eV, nearly identical to that of LDD-F(6,5) (1.049 eV), consolidating our hypothesis. Notably, the spatial distributions of HOMO and LUMO in G-modified CNTs are markedly different from those observed for sp^3 defect-modified CNTs. Previous DFT studies on sp^3-defect modified CNTs have shown that their HOMO and LUMO were delocalized between the functional groups and CNT framework, resulting in pronounced changes in the electron density of the CNT framework (*13*, *51*). Instead, our DFT results suggest that the electron density on the CNT framework with guanine-defects remains largely unchanged (Fig. 2A). These findings further support that the sp^2 defects cause minimal disruption to the π-conjugation system of the nanotube framework.

The DFT analysis has offered valuable insights into the electronic structures of sp^2 defect-modified CNTs in their ground states. To further explore the electronic properties of these modified tubes in excited states, we conducted femtosecond transient absorption (TA) experiments. TA spectroscopy monitors the temporal evolution of excited-state populations across various energy levels, providing information on carrier relaxation and recombination processes following photoexcitation (*52*–*54*). Figure 2, C and F, displays the 2D and 1D TA spectra of pristine (6,5) CNTs, showing the differential absorption (ΔA) as a function of pump-probe delay time. A prominent negative peak around 988 nm was observed, corresponding to the ground-state bleach (GSB) at the E_{11} transition for pristine (6,5). This peak manifests as a negative signal arising from the transient depletion of the ground-state population following photoexcitation (*55*). At 0 ps, electrons were excited from the valence band (VB) to the conduction band (CB). The initial GSB wavelength matches the value observed in the steady-state absorption spectrum (988 nm), marked with black arrows as a reference. The GSB intensity increased rapidly, reaching its maximum at 1.2 ps, indicating the saturation of

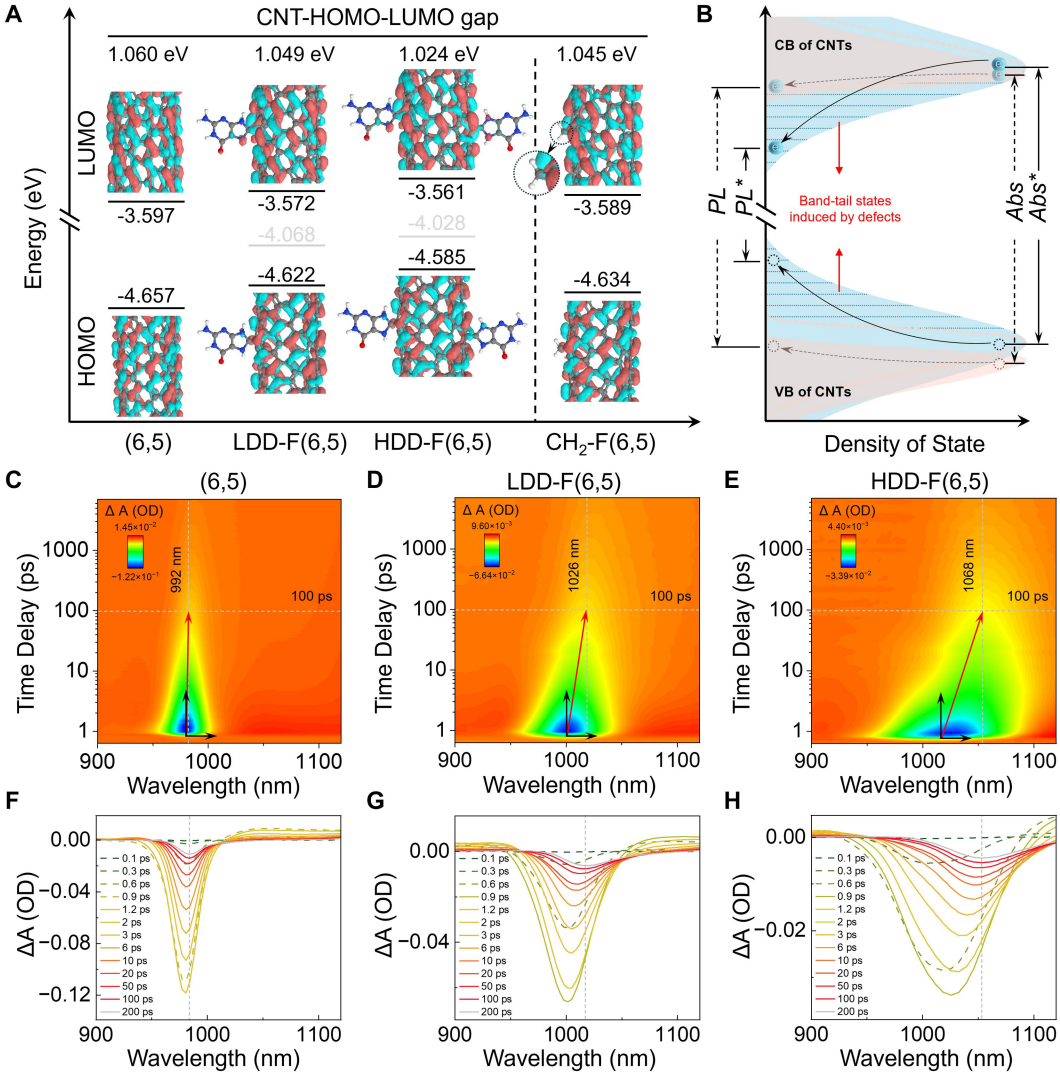

Fig. 2. DFT calculations and transient absorption (TA) spectroscopy. (**A**) DFT calculations on pristine and modified (6,5) CNTs with varying defect density. The black and gray energy levels correspond to the CNT framework and guanine functional groups, respectively. Note that CH_2-F(6,5) represents the (6,5) CNTs functionalized by a -CH_2 group. (**B**) Schematic of electron transition, relaxation and recombination pathway in pristine and modified CNTs. The pink and blue regions represent the VB/CB of pristine and modified CNTs, respectively. Dashed and solid line arrows indicate the electron relaxation pathways in pristine and modified CNTs, respectively. The shaded regions in modified CNTs represent the band-tail states induced by guanine-defects. (**C** to **E**) 2D TA spectra of (6,5), LDD-F(6,5), and HDD-F(6,5). The gray crossed dashed lines indicate the PL peak positions at the steady-state. The black arrows highlight the steady-state absorption peak positions, while the red arrows illustrate the gradual red-shifting of the GSB over time. (**F** to **H**) Early-time (0.1 ps to 200 ps) 1D TA spectra of (6,5), LDD-F(6,5), and HDD-F(6,5). The vertical dashed lines mark the steady-state PL peak positions.

excited electrons (Fig. 2F). Between 1.2 ps and 100 ps, the GSB intensity gradually decreased and underwent a slight redshift (Fig. 2F), as indicated by the red arrow in Fig. 2C. After 100 ps, no further redshift was observed, and the excited electrons relaxed at a constant wavelength of 992 nm, which corresponds to the emission wavelength in the steady-state PL spectrum. Upon modification, a similar relaxation dynamic was observed, but a much more pronounced redshift was detected. The extent of red-shifting increased with defect density (Fig. 2, D and E and G to H). Specifically, the GSB peak of LDD-F(6,5) shifted from 1002 nm to 1026 nm at 100 ps, while that of HDD-F(6,5) shifted from 1024 nm to 1068 nm.

The guanine defect-modified CNTs exhibit one set of unimodal, red-shifting GSB peaks, which distinctly differs from the behavior observed with sp^3 defects (*53*, *54*). In the latter case, two sets of unshifted GSB peaks are typically observed—one corresponding to the intrinsic energy level E_{11} of the CNT, and the other associated with the defect-induced energy level E_{11}^-. The prominent red-shifting GSB observed during relaxation is noteworthy and rarely reported in modified CNTs. We attributed this redshift to the formation of band-tail states induced by the sp^2 defects, a phenomenon well documented in other luminescent materials such as perovskites (*56*, *57*). Within the band-tail states (shaded region in Fig. 2B), excited electrons progressively relax to lower energy states, while holes migrate to higher energy states. Their recombination leads to a gradual red-shifting GSB over time. Eventually, electrons that have relaxed to the lowest energy states recombine with holes that have moved to the

highest energy states (as indicated by the solid line arrow in Fig. 2B), halting the redshift and resulting in relaxation at a constant wavelength after 100 ps (denoted as PL^*). Since band-tail states are highly sensitive to defect density, an increase in defect density results in deeper tail states, leading to a more pronounced redshift. Additionally, the band-tails broaden the electronic distribution in both the VB and CB, which is reflected in the widening of the PL and absorption spectra in the modified tubes.

Taken together, the slight changes in energy levels observed after functionalization, as suggested by DFT calculations, indicate that sp^2 defects introduce shallow potential traps in CNTs (*56*, *57*), which exert minimal influence on the electronic structure of the CNT frameworks. These shallow traps also account for the absence of additional emission peaks (i.e., E_{11}^-) that are typically seen in sp^3 defect-modified CNTs. While the overall electronic structure of CNT framework remains largely unaffected, the incorporation of sp^2 defects alters the symmetry of the CNT lattice (i.e., lattice remodeling). This, in turn, broadens the sharp energy band edges of CNTs and induces the formation of band-tail states. These band-tail states create new electronic transition and recombination pathways, thereby altering both the absorption and emission characteristics of the F-CNTs. The time-dependent red-shifting and broadening of the GSB peaks observed in the TA spectra strongly support this conclusion.

Tailoring the optical properties of CNTs by inverse design of guanine-defects

The results above reveal the fundamental mechanisms by which guanine-defects alter the lattice structure of CNTs, thereby changing their electronic properties. Since CNTs exhibit chirality-dependent lattice structures, this opens up ample possibilities for manipulating their properties. To explore this further, we selected four distinct species– (9,1), (8,3), (6,5), and (7,5)–for systematic investigation. DNA sequences with varying G contents (6.7%, 13.3%, 20%, 26.7%, and 33.3%, table S1) were employed to modulate the defect density. The G bases are evenly distributed within each sequence to minimize potential effects arising from the defect distribution pattern. The PL and Raman spectra of the modified CNTs are illustrated in Fig. 3, A and B. These four CNT species displayed varying degrees of PL-peak shifts and D-peak enhancements as the G content increased. For instance, at a G content of 33.3%, the observed PL peak shifts were 70 nm for (6,5), 40 nm for (7,5), 26 nm for (8,3), and 10 nm for (9,1). The corresponding I_D values were 0.40 for (6,5), 0.37 for (7,5), 0.31 for (8,3), and 0.09 for (9,1), respectively. Figure 3, C and D, depict the variation of $\Delta\lambda\left(\lambda_{PL^*}-\lambda_{PL^0}\right)$ and I_D with respect to the G content, where λ_{PL^*} and λ_{PL^0} represents the PL wavelengths of modified and pristine CNTs, respectively (see fig. S14 for detailed analysis). All four CNTs demonstrate a strong linear correlation ($R^2 > 0.97$), with the slopes of the fitting lines denoted as $k_{\Delta\lambda}$ and k_D. Notably, both $k_{\Delta\lambda}$ and k_D followed a similar trend: k (6,5) > k (7,5) > k (8,3) > k (9,1). Given that (6,5) and (9,1) have the same diameter, this observation challenges the conventional understanding that the spectral variation of modified CNTs is inversely proportional to their diameter (*10*, *11*, *58*).

To understand the chirality-dependent spectral variations induced by defects across various CNTs, we present the following analysis. Previously, we proposed that guanines preferentially react with the carbon-carbon (C-C) bonds along the armchair line of CNTs (*16*). In this study, our calculations show that these armchair C-C bonds do exhibit greater curvature and larger σ-π angles than the other two types of C-C bonds (figs. S15 and S16). These geometric features render the armchair C-C bonds more reactive. To facilitate a quantitative assessment, and drawing upon established correlations between emission shifts in G-modified CNTs and local bond curvature (*28*), we used the curvature (C) of the armchair line as an indicator of the average effect of each guanine-defect on CNT properties. This approach is justified as C directly reflects the local bending of C-C bonds (Fig. 3E, left panel). A higher C corresponds to a larger $\angle\sigma\pi$, indicating a concomitant increase in bond energy (fig. S16 and table S2). Consequently, the incorporation of defects into these C-C bonds will exert a more pronounced impact on the CNT properties. The following equations (Eqs. 1 to 3) quantify C, with the derivation process detailed in fig. S17

$$C(n,m)=\frac{2D}{D^2+\frac{h^2}{\pi^2}} \tag{1}$$

$$D=\frac{a\sqrt{n^2+m^2+nm}}{\pi} \tag{2}$$

$$h=a\sqrt{n^2+m^2+nm}\tan\left[30^\circ-\cos^{-1}\left(\frac{2n+m}{2\sqrt{n^2+m^2+nm}}\right)\right] \tag{3}$$

where D is the CNT diameter, h is the pitch of armchair line, a is the lattice constant of a graphene, $a = 2.46$ Å (*37*), n and m are chirality index of CNTs. Both D and h are functions of the chirality indices (n, m). Based on Eqs. 1 to 3, the C values for the (9,1), (8,3), (6,5), and (7,5) CNTs were calculated to be 0.220, 0.242, 0.267, and 0.242 $Å^{-1}$, respectively. Among them, $C(6, 5)$ is the largest, indicating that defects have a more pronounced impact on the (6,5) tubes. This explains why the modified (6,5) shows a more pronounced PL redshift and a stronger D-peak compared to other modified CNTs. Conversely, $C(9, 1)$ exhibits the lowest value, accounting for its relatively minor spectral variation after modification.

Note that (8,3) and (7,5) share an identical C value, which does not interpret their differences observed in Fig. 3, A to D. To understand this discrepancy, we considered another factor: the number of defects (N) within a *unit length* of CNT (Fig. 3E, right panel). For a given reactive DNA sequence with a fixed G content, N is proportional to the D of CNTs, as larger tubes require more DNA to wrap around them (see further discussion in fig. S19). Thus, N also depends on the chirality indices (n, m), and can be expressed as Eq. 4

$$N(n,m)\propto\pi\times\left(D+2d_{\pi-\pi}\right) \tag{4}$$

where $d_{\pi-\pi}$ is intermolecular distance between nucleobases and CNT surface, which is approximated as $d_{\pi-\pi}= 3.3$ Å (*59*, *60*).

By combining the contribution of C and N, we define a modification index, $M(n, m)$, to assess the overall impact of guanine-defects on the properties of modified CNTs. This index considers both the effect of individual defect and their density per unit length, and can be expressed as Eq. 5

$$M(n,m)\propto C(n,m)\times N(n,m)$$
$$=\frac{2a\pi\sqrt{n^2+m^2+nm}+4\pi^2d_{\pi-\pi}}{a\sqrt{n^2+m^2+nm}\left\{1+\tan^2\left[30^\circ-\cos^{-1}\left(\frac{2n+m}{2\sqrt{n^2+m^2+nm}}\right)\right]\right\}} \tag{5}$$

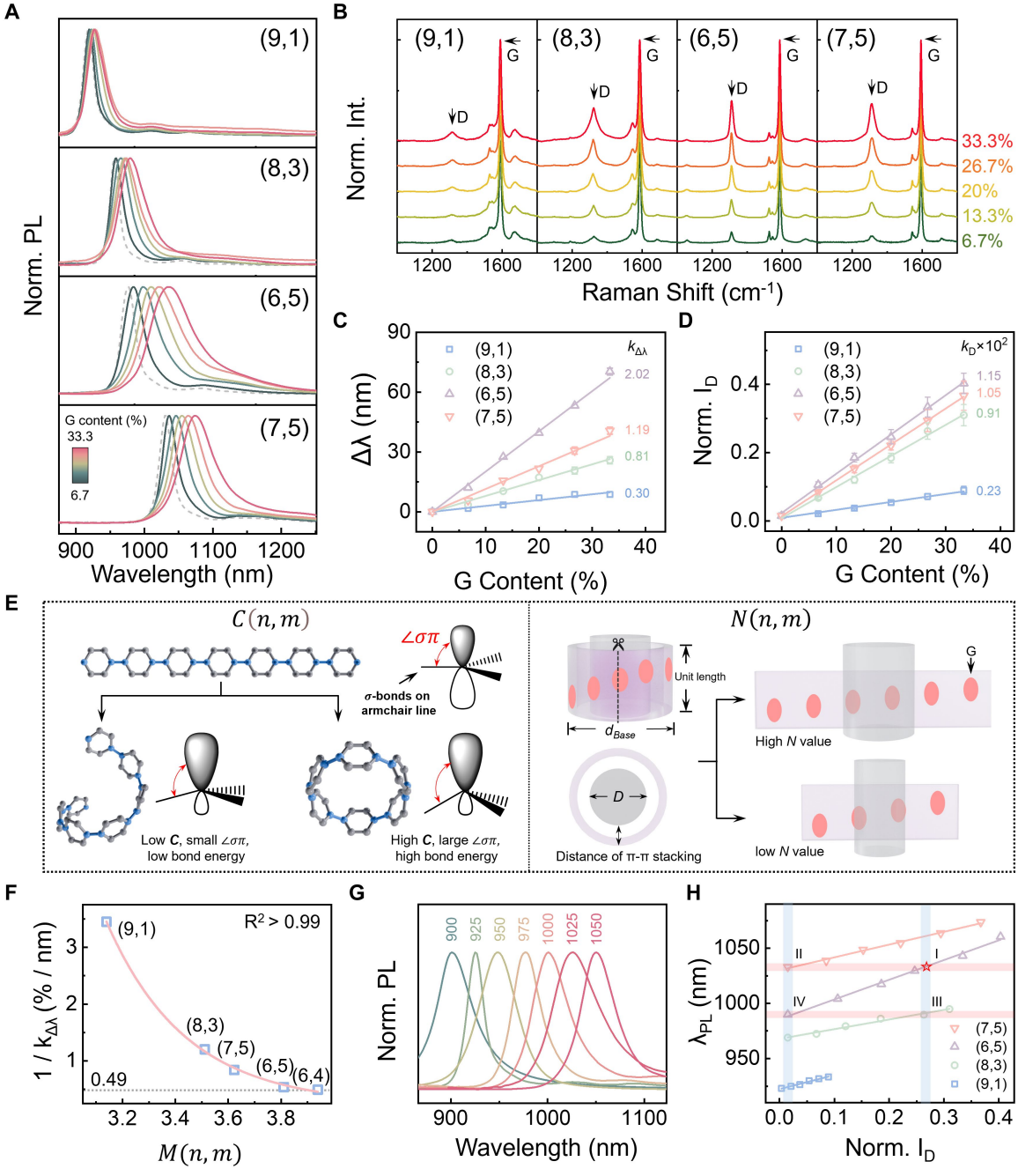

Fig. 3. Precise modulation of CNT properties through guanine-defect design. (**A**) PL and (**B**) Raman spectra of four F-CNTs with varying defect densities, modulated by DNA sequences with G contents of 6.7%, 13.3%, 20%, 26.7%, and 33.3%, respectively. The dashed lines in panel **A** represent the PL spectra of pristine CNTs. (**C** and **D**) Linear fits of the PL shift (Δλ) and Raman I_D with the G content, where Δλ denotes the PL wavelength difference between pristine and modified CNTs for each species. Data points in panels (C) and (D) represent the mean of three independent measurements. (**E**) Schematic illustration showing how *C* (*n*, *m*) and *N* (*n*, *m*) affect the properties of G-modified CNTs. (**F**) Relationship between $1/k_{\Delta\lambda}$ and *M* (*n*, *m*), where $1/k_{\Delta\lambda}$ represents the G content (%) required to induce a 1-nm redshift in PL after functionalization. The curve was fitted with an inverse function ($R^2 > 0.99$). (**G**) Experimentally measured PL spectra of seven F-CNTs with targeted λ_{PL} values of 900, 925, 950, 975, 1000, 1025, and 1050 nm. The resulting λ_{PL} values were 901, 925, 949, 976, 1001, 1026, and 1050 nm (fig. S24), respectively, in excellent agreement with the intended targets. (**H**) Linear fit of λ_{PL} versus I_D for four F-CNTs ($R^2 > 0.98$). Pink horizontal reference lines indicate samples with the same λ_{PL} but different I_D values, while blue vertical reference lines indicate samples with identical I_D but different λ_{PL}. Experimental data for intersection I, marked by a red pentagram, was obtained through defect design in CNTs (fig. S27), which corresponds to the F(6,5) with $\lambda_{PL} = 1029$ nm and $I_D = 0.27$.

A higher $M(n, m)$ value indicates a more pronounced defect effect, leading to a larger PL redshift and a stronger D-peak. We then quantified the $M(n, m)$ values for four CNTs, which follow the order: $M(6, 5) > M(7, 5) > M(8, 3) > M(9, 1)$. This trend is in excellent agreement with the observed behaviors for $k_{\Delta\lambda}$ and k_D, as shown in Fig. 3, C and D. To further test the robustness of $M(n, m)$, we calculated the value for an untested CNT, $M(6, 4)$, which was found to be higher than that of $M(6, 5)$. This implies that the modified (6,4) should exhibit larger $k_{\Delta\lambda}$ and k_D values compared to (6,5). Experimental results for the modified (6,4) yielded $k_{\Delta\lambda} = 2.03$ and $k_D = 0.0124$ (figs. S20 and S21), both of which exceeded the corresponding values of F(6,5), 2.02 and 0.0115. These findings indicate that the $M(n, m)$ effectively predict the impact of defects on CNT properties.

The understanding of how guanine-defects affect various (n, m) CNTs allows us to customize the optical properties of modified CNT through defect design. To facilitate this, we plotted $1/k_{\Delta\lambda}$ as a function of $M(n, m)$, where $1/k_{\Delta\lambda}$ represents the G content (%) required to induce a 1-nm redshift in PL after functionalization. As shown in Fig. 3F, it exhibits a strong inverse proportional correlation ($R^2 > 0.99$). The relationship between $M(n, m)$ and $1/k_D$ was plotted in fig. S22. These correlations provide a powerful platform for designing defects in selected (n, m) CNTs to achieve predetermined λ_{PL} and I_D.

We first demonstrate the ability to precisely tune the λ_{PL} of modified CNTs. For instance, to achieve a target λ_{PL*} of 900 nm, we started with pristine (6,4) CNTs, which exhibit an initial λ_{PL} of 885 nm. By inducing a redshift of 15 nm, the target λ_{PL*} could be reached. As shown in Fig. 3F, a G content of 0.49% produces a 1-nm redshift in the λ_{PL} of modified (6,4); therefore, achieving the full 15-nm redshift requires a DNA sequence with a G content of 7.35%. Based on this, we designed the $C_6GC_{13}GC_7$ sequence to functionalize (6,4) CNTs. The resulting PL spectrum of F (6,4) is shown in fig. S23, with $\lambda_{PL*} = 901$ nm, aligning well with the target value.

In principle, this approach enables the synthesis of F-CNT with any desired λ_{PL*}. To further validate this strategy, we designed and synthesized six additional F-CNTs with target λ_{PL*} of 925, 950, 975, 1000, 1025, and 1050 nm (Fig. 3G and fig. S24). The detailed design protocol is outlined in fig. S24H. The experimentally measured λ_{PL*} values closely match the targets, with an error margin of only ±1 nm. A particularly noteworthy result is the successful design of F-CNTs with $\lambda_{PL} = 1025$ nm using the (7,3) species—a chirality for which no prior experimental data regarding guanine-based covalent functionalization was available. Our model accurately predicted how defects would influence the PL of F(7,3) (fig. S25), and the experimental results were in excellent agreement with these predictions (fig. S24F).

Beyond designing λ_{PL*}, our approach also enables precise control over the I_D of F-CNTs. For example, by targeting an I_D value of 0.2, various CNTs can be modified to achieve the desired outcome. Figure S26 shows the Raman spectra of the modified (7,3), (6,4), and (6,5), with measured I_D values of 0.198, 0.201, and 0.198, respectively. These results closely match the target, with an average error below 1%. These findings, combined with the λ_{PL*} modulation discussed above, validate the accuracy and reliability of our approach for encoding CNT properties through rational defect design.

Since both λ_{PL} and I_D of F-CNT are directly correlated with defect density, we incorporated them into a plot to better illustrate their relationship. As shown in Fig. 3H, a strong linear correlation was observed across all four CNTs. By adding vertical and horizontal reference lines, we pinpointed specific F-CNT samples at the intersection, where the λ_{PL} and I_D values match those of two other samples. For instance, at intersection II, its λ_{PL} is identical to that of I, while its I_D matches that of IV. These unique orthogonal dual-optical signals at the intersection present exciting opportunities for the application of G-modified CNTs, which will be discussed further in the next sections.

Four intersections were identified in Fig. 3H, with the intersection I—marked by a red pentagram—corresponding to a λ_{PL} of 1029.8 nm and an I_D of 0.268. However, experimental data for this point were not available in Fig. 3, C and D. To address this gap, we customized an F-CNT by reacting $C_2(GC_4)_4GC_3GC_2$ with pristine (6,5). The resulting F(6,5) exhibited a λ_{PL} of 1029 nm and an I_D of 0.270 (fig. S27), effectively bridging the data gap. This example further underscores the accuracy of our defect-design strategy in tailoring the optical properties of CNTs.

Tailored guanine defect-modified CNTs for pattern switching

The results above highlight the distinctive role of guanine-defects in modulating the electronic properties of CNTs, particularly in the precise control of PL and Raman profiles. In the following two sections, we explored the applications of these precisely tuned CNTs. We first demonstrate their use in pattern switching, utilizing the four samples identified by the intersections in Fig. 3H. Sample information and corresponding PL and Raman spectra are presented in Fig. 4, A to C. These samples exhibit identical λ_{PL} but distinct I_D values, and vice versa. This dual-optical behavior is key to pattern switching, as it allows for orthogonal control of optical signal output during PL and Raman mapping.

As a proof of concept, we constructed a 2 × 4 sample plate with 8 wells, into which four types of CNTs samples were injected in a predefined order (Fig. 4D). PL and Raman mapping experiments were then performed on this plate. During imaging, each well generated a color block or pixel. For data analysis, PL wavelengths from 990 to 1029 nm were mapped onto a green color scale, from dark to light, while I_D values from 0 to 0.27 were mapped onto a blue color scale (Fig. 4E). As a result, in PL imaging mode, samples I and II appeared as lighter green blocks whereas samples III and IV formed darker green blocks, creating a "Z-shaped" pattern (Fig. 4F). In Raman imaging mode, samples I and III displayed lighter blue blocks, while samples II and IV appeared as darker blue blocks, producing a "chessboard-like" pattern.

To demonstrate the capability to image and switch more complex patterns, a 20 × 20 sample plate with 400 pixels was employed. The increased number of pixels allowed the creation of higher-resolution patterns. The assignment of CNT samples in each well across the plate is illustrated in figs. S28 to S32. To better showcase the outcome, five 20 × 20 plates were arranged into an array, with each plate displaying a distinct pattern. In PL imaging mode, the array displayed the letter pattern "CHINA", whereas in Raman imaging mode, the pattern switched to "WORLD." The precise conversion between these patterns highlights that the signal from each pixel was orthogonally controlled by the PL and Raman of CNTs. We emphasize that, in principle, this method can be extended to generate arbitrary patterns with customizable resolution by adjusting the number of pixels and the variety of CNTs.

Tailored guanine defect-modified CNTs for multi-layer information encryption

In this section, we demonstrate the use of guanine defect-modified CNTs for multi-layer information encryption, an application that

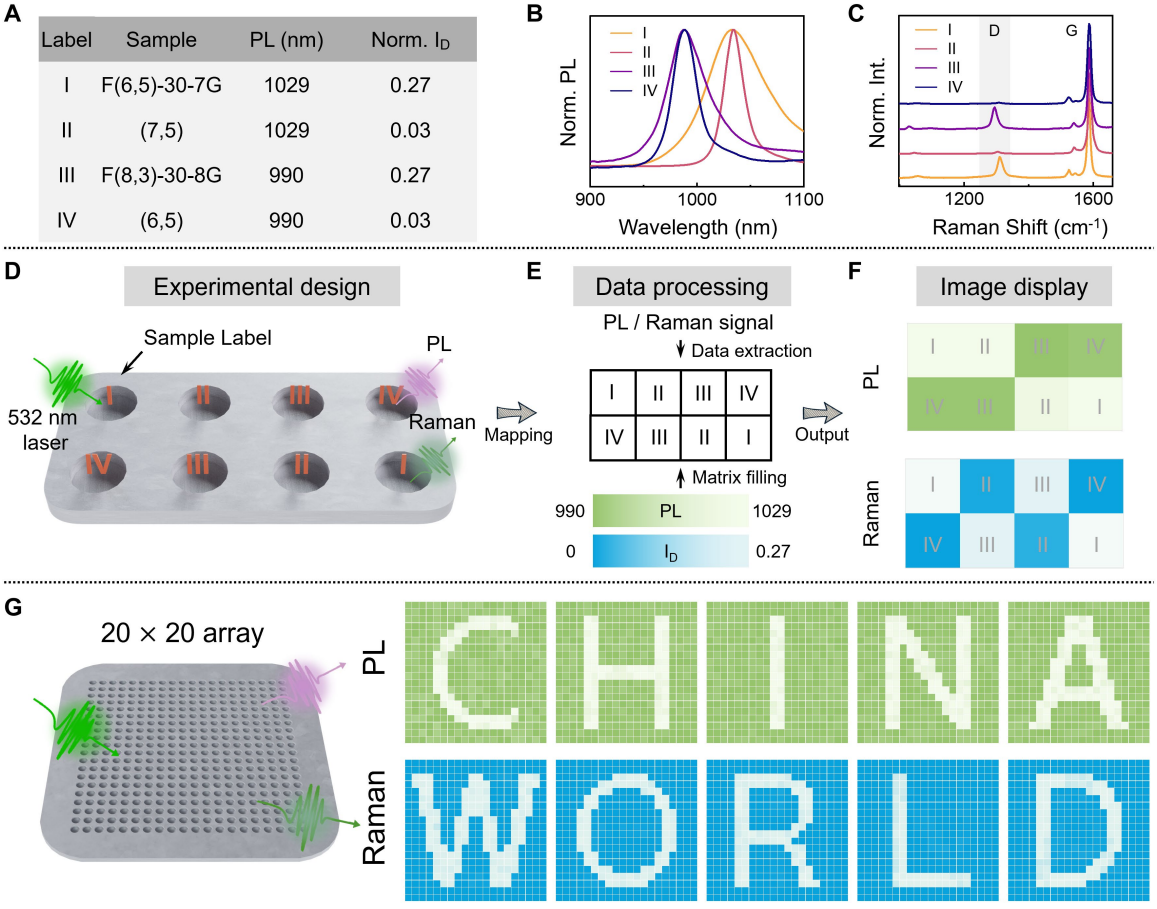

Fig. 4. Tailored guanine defect-modified CNTs for pattern switching. (**A**) Overview of the four samples identified by the intersections in Fig. 3H. (**B**) PL and (**C**) Raman spectra of the four samples. (**D**) Schematic of the PL and Raman imaging setup. The imaging plate consists of 8 wells, each with a 4 mm diameter and 5 mm center-to-center spacing between adjacent wells. Each well was filled with 5 μL of sample solution. A 532 nm laser was directed vertically into the wells to sequentially collect the PL and Raman signals, with automated software controlling the movement between wells. (**E**) Data processing workflow, where λ_{PL} and Raman I_D values were extracted from the collected signals, mapped to false-colors, and used to generate the patterns. (**F**) Various patterns obtained from PL and Raman imaging. Note that the gray numbers are sample indices, not derived from imaging. (**G**) Higher-resolution imaging with a 20 × 20 sample plate. Five plates were arranged into an array, with the PL images displaying the word "CHINA" and the Raman images displaying "WORLD."

extends the programmable tuning capabilities established in the preceding section. This encryption platform serves as a rigorous 'stress test' for the precision and stability of our functionalization methodology. By generating spatial patterns with orthogonal PL and Raman profiles, we provide a tangible validation of the unprecedented level of structural control afforded by our inverse-design strategy.

While optical encryption has been extensively studied (*61*–*66*), we propose a distinct multi-layered encryption system that substantially enhances information security. Much of the field employs ultraviolet and/or visible (UV-vis) light for encryption (*62*, *64*, *65*, *67*), which are susceptible to facile detection and decryption. In contrast, our platform leverages the inherent confidentiality of the near-infrared (NIR) window and vibrational Raman signatures. The combined utilization of these two independent optical channels substantially increases the complexity of unauthorized decryption, demonstrating the robust utility of precision CNT functionalization.

Figure 5A illustrates the encryption process and its underlying principle. First, the text information to be encrypted is converted into a character string (e.g., ASCII code) and organized into an $n \times n$ pixel array, forming a character matrix [Fig. 5A (i) to (iii)]. Following a predefined rule (e.g., 0 = dark pixel, 1 = light pixel), the character matrix is transformed into a pixelated pattern, forming the information-carrying layer [Fig. 5 (A) to (iv)]. Next, an interference layer is incorporated, which can be an arbitrarily selected image. Using a panda image as an example, we first convert it into a pattern with the same pixel count as the information carrying layer, forming the interference pattern [Fig. 5 (A) to (vi)]. This interference layer is then overlaid onto the information carrying layer, creating a superimposed pattern that contains both the encrypted and interference information. Finally, based on the superimposed pattern, we design and encode the CNT sample matrix to complete the encryption process. To make our encryption protocol readily accessible, we have developed a Python software tool [InfoEncrypt Compiler] (*68*) that integrates all the design steps, from encoding the text message to generating the CNT sample matrix. Users simply need to upload a text message and an image to be encrypted, and the CNT sample matrix will be generated automatically. A detailed demonstration of the encryption process using this tool is provided in fig. S33.

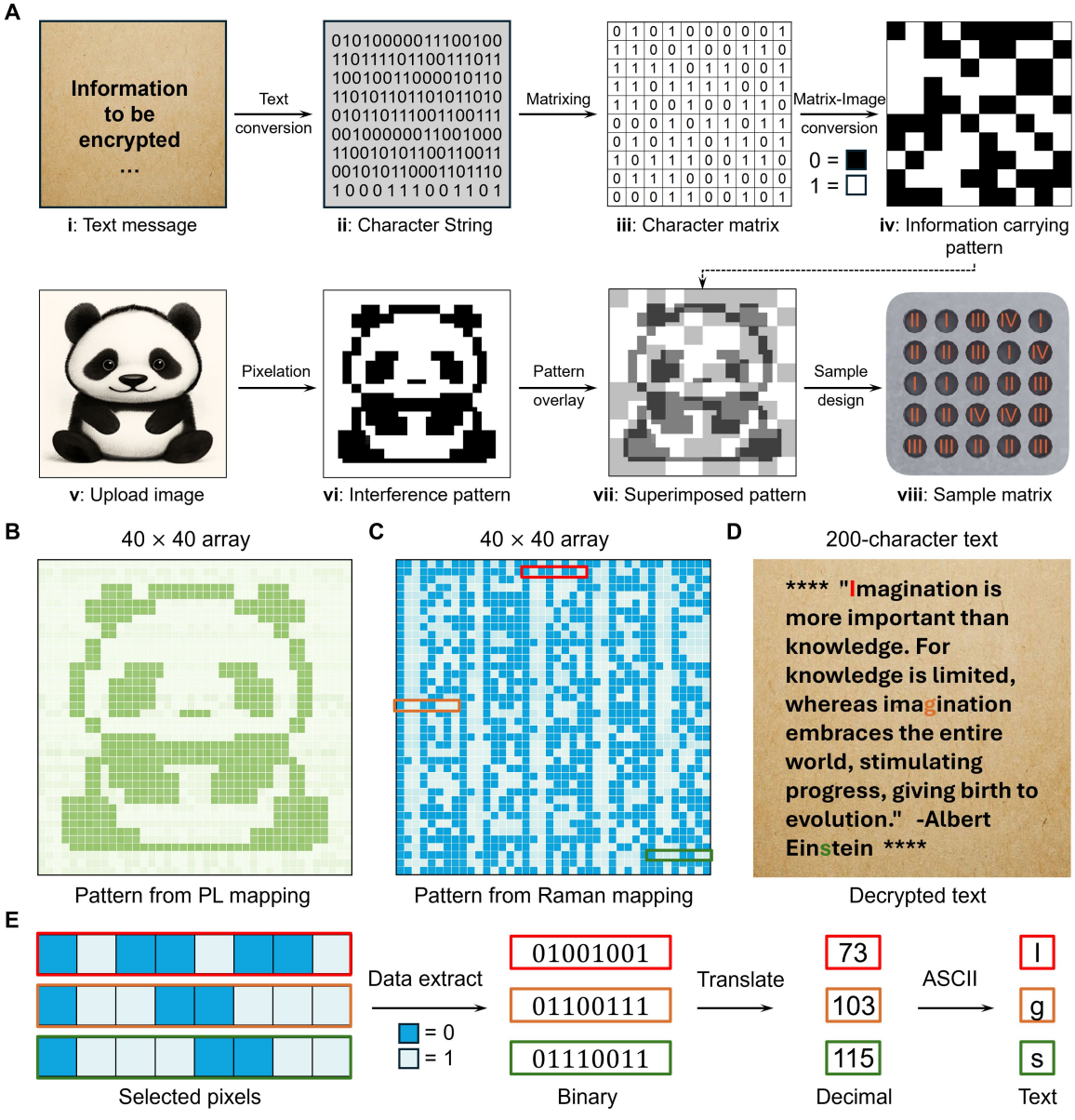

Fig. 5. Tailored guanine defect-modified CNTs for multi-layer information encryption. (**A**) Schematic illustration of the encryption process and its underlying principle. The encryption workflow is facilitated using the [InfoEncrypt Compiler] software package developed by us. (**B** to **D**) Experimental results of encrypting an Einstein quote into a 40 × 40 CNT matrix, with a panda image serving as the interference layer: (B) Pattern derived from PL mapping, which corresponds to the interference pattern. (C) Pattern derived from Raman mapping, which corresponds to the information-carrying pattern, and (D) Text information decrypted from the pattern in panel (C). (**E**) Demonstration of the decryption process. Three representative regions in panel (C) were selected for demonstration. Each region consists of eight consecutive pixels, marked in red, orange, and green in panels (C) and (D).

To experimentally test the method described above, we encrypted a famous quote by Einstein into a 40 × 40 CNT matrix, using a panda image as the interference layer. Fig. 5, B and C show the experimental results. In the PL imaging mode, a panda pattern was clearly visible (Fig. 5B), in line with our design. Meanwhile, the Raman imaging mode revealed a QR-code-like pattern (Fig. 5C), corresponding to the information-carrying layer. The QR-code-like pattern can be decoded by following the protocol outlined in the upper panel of Fig. 5A, but in a reverse order. It was first converted into a character matrix, then into a character string, and finally into text. Upon decryption, the entire sentence was revealed (Fig. 5D): **** "Imagination is more important than knowledge. For knowledge is limited, whereas imagination embraces the entire world, stimulating progress, giving birth to evolution." -Albert Einstein ****. This quote decrypted from Fig. 5C exactly matches the pre-encrypted message in the CNT sample matrix.

Figure 5E interprets the decryption process. Three representative regions in the Raman pattern were selected, each consisting of eight consecutive pixels, marked in red, orange, and green, respectively. Following the established rule that dark blue pixels represent "0"

and light blue pixels represent "1," these pixels were converted into binary character strings: "01001001," "01100111," and "00100010." These binary strings can then be transformed into decimal numbers, "73," "103," "115," respectively. According to the ASCII table, these numbers correspond to the characters "I," "g," and "s" (fig. S35). By applying this protocol to all pixels in Fig. 5C, the entire quote-including punctuation-was successfully decoded. The encryption and decryption processes are both straightforward and rigorous, forming a seamless, closed-loop system.

DISCUSSION

In summary, we have developed an inverse sp^2 defect design strategy to precisely encode the optical properties of carbon nanotubes (CNTs) using guanine chemistry. The combination of experimental and theoretical investigations elucidated the structural features of sp^2 defects and the mechanisms by which they govern the properties of modified CNTs. In contrast to conventional sp^3 defects, these sp^2 defects largely preserve the electronic structure of the CNT frameworks while modulating their properties through lattice remodeling. Through a systematic study of sp^2 defects in five distinct single-chirality CNT species, we established a chirality-dependent modification index, $M(n, m)$, which accurately describes the effects of defects on various (n, m) CNTs, even in the absence of prior experimental data [e.g., for the (7,3) species]. The index facilitates the rational predesign of defects, enabling the precise tailoring of CNTs' optical properties with unprecedented accuracy. This signifies a fundamental shift in the engineering of defects in CNTs, moving away from conventional trial-and-error approaches and retrospective characterization methods towards a more deterministic and predictive framework for materials design. The resulting defect-engineered CNTs, exhibiting orthogonal PL and Raman signatures, were employed in pattern switching and multi-layer information encryption.

Beyond these demonstrations, the capacity to engineer a vast, programmable library of high-resolution "optical barcodes" holds great potential for advanced analytics. The precisely-tailored patterns shown in Fig. 5, B and C highlight the utility of modified CNTs in multiplexed detection. This workflow can be seamlessly integrated into assays to generate distinct fingerprinting signals, enabling the simultaneous resolution of multiple analytes (*8*). Crucially, the multilayered optical signatures of these modified CNTs enhance both sensitivity and specificity—a vital advantage when navigating complex biological matrices prone to interference. We are currently leveraging these innovative materials for perception-based biofluid sensing in disease diagnostics (*22*, *69*), where rapid biomarker identification is paramount. We envision that the integration of structurally-defined CNTs into bioassays represents a promising advancement in biosensing (*70*), paving the way for more effective disease diagnosis and enhanced monitoring of health conditions. This work not only standardizes the precise tuning of CNT optical properties but also lays the groundwork for next-generation optoelectronic devices and biochemical sensing platforms.

MATERIALS AND METHODS

Materials

CoMoCAT SWCNT powders (tradename SG65i) were obtained from Sigma-Aldrich. Oligomers of ssDNA were purchased from Sangon Biotech. Polyethylene glycol [PEG; molecular weight (MW), 6 kDa; Alfa Aesar], potassium phosphate dibasic (K_2HPO_4, J&K Scientific), potassium phosphate monobasic (KH_2PO_4, J&K Scientific), phosphoric acid (H_3PO_4, 85%, J&K Scientific), sodium phosphate dibasic (Na_2HPO_4, J&K Scientific), sodium phosphate monobasic (NaH_2PO_4, J&K Scientific), sodium chloride (NaCl, J&K Scientific), sodium thiocyanate (NaSCN; Sigma-Aldrich), sodium phosphate buffer solution (NaPB; 1 M, pH = 7.4, Sigma-Aldrich), sodium deoxycholate (SDC, Sigma-Aldrich), and rose bengal (RB, dye content 95%, Sigma-Aldrich) were used as received.

Purification of single-chirality CNTs

Following previously reported procedures (*35*, *36*), DNA-CNT dispersions were prepared by sonicating SG65i SWCNT powders (1 mg) with DNA oligonucleotides (2.5 mg) in 1 mL of buffer solution. The choice of buffer depended on the target chirality: sodium phosphate buffer (30 mM, pH = 4) was used for $C_3(CCG)_3$-(9,1), $(T_3C_3)_2C_3$-(8,3), $(C_3G)_2C_4$-(7,3), $(GCCC)_3G_2C_2$-(6,4), while sodium chloride solution (30 mM) was employed for $C_3GC_6GC_4$-(7,5) and $TTA(TAT)_2ATT$-(6,5).

DNA-wrapped single-chirality CNTs were sorted using the well-established aqueous two-phase (ATP) technique (*33*, *34*). $TTA(TAT)_2ATT$-(6,5), $C_3(CCG)_3$-(9,1), $(T_3C_3)_2C_3$-(8,3) and $C_3GC_6GC_4$-(7,5), were purified following our previously reported protocols (*52*, *71*). $(GCCC)_3G_2C_2$-(6,4) and $(C_3G)_2C_4$-(7,3) were purified using an adapted ATP system, containing PEG 6 kDa, $NaH_2PO_4{\bullet}H_2O$ and $Na_2HPO_4{\bullet}7H_2O$. In the 7:3 stock solution, their respective mass fractions were 12.3%, 4.43%, and 12.2%, respectively.

The purification process involved mixing 3 volumes (60 μL) of DNA-CNT dispersions with 7 volumes (140 μL) of the 7:3 stock solution. After vortexing, the mixtures were centrifuged to collect the top fraction (1 T), which contained highly pure single-chirality CNTs. To isolate the purified DNA-CNT species, precipitation was induced by introducing 0.5 M NaSCN, followed by centrifugation at 17,000 g for 3 minutes. The pellets were then resuspended in the appropriate medium: ultrapure H_2O for optical characterization or NaPB buffer for chemical modification.

CNT functionalization by guanine chemistry

CNT functionalization was performed using a protocol adapted from a previously reported one-pot methodology (*16*). The following procedure outlines a representative reaction, using 30-1G $(C_{14}GC_{15})$-functionalized (6,5) as an example. The reaction mixture was prepared by combining 5 μL of $TTA(TAT)_2ATT$-(6,5) (OD ~25), 5 μL of NaPB buffer (20 mM, pH = 7.4), 2 μL of 10% SDC, and 5 μL of 30-1G DNA (10 mg/mL), followed by vortexing. This initial step resulted in complete replacement of $TTA(TAT)_2ATT$ with SDC. Subsequently, 100 μL of MeOH was added dropwise under vigorous vortexing conditions (5 μL per drop for 10 additions, followed by 10 μL per drop for 5 additions). During this MeOH addition, SDC was displaced from the (6,5) CNTs, while 30-1G DNA were wrapped onto the nanotube surfaces. The reaction conditions were then adjusted by adding 81 μL of NaPB buffer (20 mM, pH = 7.4) and 2 μL of RB (6 mM) to give a final MeOH content of 50% v/v. The final concentration of RB was maintained at 60 μM, providing a twofold excess over the established functional threshold (20–30 μM) to ensure optical reaction efficiency (*28*). The complete reaction mixture, placed in a 2 mL glass vial, was illuminated with paired 525 nm LED lamps (PR160 Rig with Fan kit, Kessil) for 1 hour at room temperature.

Following the photochemical reaction, the functionalized CNTs were isolated by precipitating with NaSCN (added from a 5 M stock to a final concentration of 0.5 M) and centrifuging at 17,000 g for 3 minutes). After complete removal of the supernatant, the pellets were resuspended in 20 mM NaPB buffer (pH = 7.4) for subsequent characterization.

It is important to note that reaction outcomes—specifically the relationship between spectral shifts and guanine (G) content—can be influenced by parameters such as RB concentration, irradiation flux, and temperature. To ensure the reproducibility and transferability of the observed slopes (Fig. 3), all reactions in this study were conducted under a standardized 'reaction-to-completion' protocol. By utilizing a saturating RB concentration (60 μM) and an irradiation duration (60 min) that substantially exceeds the observed kinetic plateau (see fig. S3), we ensure the functionalization reaches a stoichiometric limit. Under these optimized conditions, the modification index, M(n, m), becomes an intrinsic property of the DNA-CNT conjugate, independent of minor variations in the experimental setup.

UV-Vis-NIR absorption spectroscopy

UV-Vis-NIR absorption measurements were carried out on a Hitachi UH-5700 spectrophotometer using a quartz microcuvette with 1 cm path length. Spectra were acquired in the wavelength range of 350–1350 nm, and background correction was applied to each spectrum.

Steady-State PL spectroscopy

PL spectra were acquired using the NS Super NanoSpectralyzer from Applied NanoFluorescence (Houston, TX), employing an excitation wavelength of 660 nm.

Excitation-Emission spectroscopy

Two-dimensional Excitation-Emission spectra were collected using the Edinburgh FLS1000. An automated excitation-emission matrix was generated with the FLS1000's Fluoracle software. The excitation wavelength was scanned from 500 nm to 650 nm in 10 nm steps, and the excitation intensity was corrected using the FLS1000's reference detector. The photoluminescence emission was measured between 900 nm and 1400 nm in a single capture using the InGaAs NIR camera.

Raman spectroscopy

Raman spectra were collected using the XploRA PLUS system, with a laser excitation wavelength of 532 nm and a power range of 1–5 mW. The functionalized CNT samples (~5 μL) were deposited onto aluminum foil. Following complete solvent evaporation, the laser was focused on the solid samples for analysis. The typical integration time is 30 s, with three accumulations per measurement. Spectra were recorded over the range of 200–1800 cm^{-1}.

Femtosecond transient absorption (TA) spectroscopy

TA experiments were performed using an integrated Helios setup (Ultrafast Systems LLC) in a nondegenerate pump-probe configuration, with a maximum time delay of approximately 7.6 ns. Pump pulses were generated by a Coherent TOPAS-C optical parametric amplifier, pumped by a 1 kHz Coherent Astrella F regenerative amplifier (800 nm, 100 fs, 7 mJ/pulse) and split into two beams. The amplifier was seeded by a mode-locked Ti-sapphire oscillator (Coherent Vitara, 30 fs, 80 MHz). The signal beam underwent twice frequency doubling using beta-barium borate (BBO) crystals to generate a 400 nm pump pulse, with the power adjusted to approximately 80 μW using neutral-density filters. The second beam was converted into a white light continuum probe pulse (820–1600 nm) via an yttrium aluminum garnet crystal, which probed the sample states after photoexcitation by the pump pulse. A 450 nm short-pass filter was placed in front of the sample to block residual light. A 400 μL sample with an optical density of approximately 1.5 was loaded into a 2 mm path length cuvette for testing.

X-ray photoelectron spectroscopy (XPS)

To remove residual Rose Bengal and free DNA, the functionalized CNT samples were purified through three cycles of precipitation, followed by three rounds of ultrafiltration using 100 kDa molecular weight cut-off centrifugal filters (Cobetter). The purified samples were ultimately concentrated to an optical density (OD) of ~20. For XPS measurements, the concentrated solutions were evenly drop-cast onto indium tin oxide (ITO) glass substrates and subsequently dried in a vacuum freeze-dryer. XPS spectra were then acquired using a ULVAC-PHI GENESIS 500 Surface Analyzer. The acquired data were processed and analyzed using MultiPak software.

PL and Raman mapping experiments

The functionalized CNT samples (as specified in Fig. 4A) were loaded into a custom-engineered aluminum alloy plate according to the predefined spatial arrays (Fig. 4D and figs. S28 to S32 and fig. S34). The mapping mold featured an $n \times n$ array of wells, each with a diameter of 4 mm, a depth of 5 mm, and a center-to-center pitch of 5 mm. Each well was filled with a 10 μL aliquot of the respective CNT dispersion, standardized to an optical density (OD) of 1–2.

PL and Raman mapping were performed independently and sequentially using a Horiba XploRA PLUS microspectroscopy system. To ensure data integrity across the entire array, the automated acquisition was structured into two distinct sessions: a complete PL mapping sequence was conducted for all sample wells, followed by a standalone Raman scanning session. To mitigate the effects of solvent evaporation and potential fluctuations in the liquid level during these extended measurements, the confocal objective was precisely focused at the bottom of the wells for both sessions.

All spectral data were collected using a 532 nm excitation laser with the power maintained at 10 mW. The specific acquisition settings were as follows. PL spectra were recorded over a range of 960–1040 nm with an integration time of 3 s per pixel. Raman signatures were captured from 1000–1800 cm^{-1} with an integration time of 1 s per pixel.

The mapping protocols were scaled according to the complexity of the encoded patterns. A 4 × 2 configuration (8 data points) was used for initial characterization (Fig. 4, D to F). A 20 × 20 configuration (400 data points) was utilized for large-scale screening (Fig. 4G). A high-resolution 40 × 40 (1600 data points) was acquired to render the spatial information maps (Fig. 5, B and C).

During acquisition, the Analysis module in LabSpec 6 processed the data in real-time. For PL-based data, the emission maxima (λ_{PL}) were automatically extracted. For Raman spectra, the I_D (normalized to I_G) was calculated by integrating the designated D-band (≈ 1280–1030 cm^{-1}) and G-band (1560–1610 cm^{-1}) region. The resulting λ_{PL} and I_G values were exported as numerical matrices, imported into Origin software, and rendered into high-resolution pseudocolor images using a predefined color-scale mapping (Fig. 4E). This automated workflow allows for the rapid decryption of complex spatial patterns without manual spectral analysis.

Computational methods

A hydrogen-capped (6,5) CNT molecular model consisting of a single unit cell was employed for DFT calculations. The model was 4.06 nm in length, comprising 16 hexagonal rings and approximately 400 atoms. The geometric optimizations were performed for pristine (6,5), LDD-F(6,5), HDD-F(6,5), and CH_2-F(6,5) CNT (see fig. S10) using the ORCA 6.0 software (*72*). These calculations utilized the PBE functional (*73*) with the def2-SVP basis set (*74*) to ensure a balanced trade-off between accuracy and computational cost. Subsequent molecular orbital visualizations were rendered using the Jmol package, enabling clear interpretation of electronic structure features.

Supplementary Materials

This PDF file includes:

Figs. S1 to S35
Tables S1 and S2

REFERENCES

1. G. L. Pearson, J. Bardeen, Electrical Properties of Pure Silicon and Silicon Alloys Containing Boron and Phosphorus. *Phys. Rev.* **75**, 865–883 (1949).
2. S. M. Sze, K. K. Ng, *Physics of Semiconductor Devices* (Wiley, ed. 1, 2006); https://onlinelibrary.wiley.com/doi/book/10.1002/0470068329.
3. F. J. Morin, J. P. Maita, Electrical Properties of Silicon Containing Arsenic and Boron. *Phys. Rev.* **96**, 28–35 (1954).
4. M. J. O'Connell, S. M. Bachilo, C. B. Huffman, V. C. Moore, M. S. Strano, E. H. Haroz, K. L. Rialon, P. J. Boul, W. H. Noon, C. Kittrell, J. Ma, R. H. Hauge, R. B. Weisman, R. E. Smalley, Band Gap Fluorescence from Individual Single-Walled Carbon Nanotubes. *Science* **297**, 593–596 (2002).
5. S. M. Bachilo, M. S. Strano, C. Kittrell, R. H. Hauge, R. E. Smalley, R. B. Weisman, Structure-Assigned Optical Spectra of Single-Walled Carbon Nanotubes. *Science* **298**, 2361–2366 (2002).
6. M. S. Strano, C. A. Dyke, M. L. Usrey, P. W. Barone, M. J. Allen, H. Shan, C. Kittrell, R. H. Hauge, J. M. Tour, R. E. Smalley, Electronic Structure Control of Single-Walled Carbon Nanotube Functionalization. *Science* **301**, 1519–1522 (2003).
7. J. D. Harvey, P. V. Jena, H. A. Baker, G. H. Zerze, R. M. Williams, T. V. Galassi, D. Roxbury, J. Mittal, D. A. Heller, A carbon nanotube reporter of microRNA hybridization events in vivo. *Nat. Biomed. Eng.* **1**, 0041 (2017).
8. Z. Yaari, Y. Yang, E. Apfelbaum, C. Cupo, A. H. Settle, Q. Cullen, W. Cai, K. L. Roche, D. A. Levine, M. Fleisher, L. Ramanathan, M. Zheng, A. Jagota, D. A. Heller, A perception-based nanosensor platform to detect cancer biomarkers. *Sci. Adv.* **7**, eabj0852 (2021).
9. S. Ghosh, S. M. Bachilo, R. A. Simonette, K. M. Beckingham, R. B. Weisman, Oxygen Doping Modifies Near-Infrared Band Gaps in Fluorescent Single-Walled Carbon Nanotubes. *Science* **330**, 1656–1659 (2010).
10. Y. Piao, B. Meany, L. R. Powell, N. Valley, H. Kwon, G. C. Schatz, Y. Wang, Brightening of carbon nanotube photoluminescence through the incorporation of sp3 defects. *Nat. Chem.* **5**, 840–845 (2013).
11. A. H. Brozena, J. D. Leeds, Y. Zhang, J. T. Fourkas, Y. Wang, Controlled Defects in Semiconducting Carbon Nanotubes Promote Efficient Generation and Luminescence of Trions. *ACS Nano* **8**, 4239–4247 (2014).
12. X. Ma, N. F. Hartmann, J. K. S. Baldwin, S. K. Doorn, H. Htoon, Room-temperature single-photon generation from solitary dopants of carbon nanotubes. *Nat. Nanotechnol.* **10**, 671–675 (2015).
13. H. Kwon, A. Furmanchuk, M. Kim, B. Meany, Y. Guo, G. C. Schatz, Y. Wang, Molecularly Tunable Fluorescent Quantum Defects. *J. Am. Chem. Soc.* **138**, 6878–6885 (2016).
14. X. He, N. F. Hartmann, X. Ma, Y. Kim, R. Ihly, J. L. Blackburn, W. Gao, J. Kono, Y. Yomogida, A. Hirano, T. Tanaka, H. Kataura, H. Htoon, S. K. Doorn, Tunable room-temperature single-photon emission at telecom wavelengths from sp3 defects in carbon nanotubes. *Nat. Photonics* **11**, 577–582 (2017).
15. A. Saha, B. J. Gifford, X. He, G. Ao, M. Zheng, H. Kataura, H. Htoon, S. Kilina, S. Tretiak, S. K. Doorn, Narrow-band single-photon emission through selective aryl functionalization of zigzag carbon nanotubes. *Nat. Chem.* **10**, 1089–1095 (2018).
16. Z. Lin, L. C. Beltran, Z. A. De los Santos, Y. Li, T. Adel, J. A. Fagan, A. R. H. Walker, E. H. Egelman, M. Zheng, DNA-guided lattice remodeling of carbon nanotubes. *Science* **377**, 535–539 (2022).
17. F. L. Sebastian, F. Becker, Y. Yomogida, Y. Hosokawa, S. Settele, S. Lindenthal, K. Yanagi, J. Zaumseil, Unified Quantification of Quantum Defects in Small-Diameter Single-Walled Carbon Nanotubes by Raman Spectroscopy. *ACS Nano* **17**, 21771–21781 (2023).
18. A. Vierck, F. Gannott, M. Schweiger, J. Zaumseil, J. Maultzsch, ZA-derived phonons in the Raman spectra of single-walled carbon nanotubes. *Carbon* **117**, 360–366 (2017).
19. F. L. Sebastian, N. F. Zorn, S. Settele, S. Lindenthal, F. J. Berger, C. Bendel, H. Li, B. S. Flavel, J. Zaumseil, Absolute Quantification of sp3 Defects in Semiconducting Single-Wall Carbon Nanotubes by Raman Spectroscopy. *J. Phys. Chem. Lett.* **13**, 3542–3548 (2022).
20. W.-L. Yim, J. K. Johnson, Ozone Oxidation of Single Walled Carbon Nanotubes from Density Functional Theory. *J. Phys. Chem. C* **113**, 17636–17642 (2009).
21. C.-W. Lin, S. M. Bachilo, Y. Zheng, U. Tsedev, S. Huang, R. B. Weisman, A. M. Belcher, Creating fluorescent quantum defects in carbon nanotubes using hypochlorite and light. *Nat. Commun.* **10**, 2874 (2019).
22. M. Kim, C. Chen, P. Wang, J. J. Mulvey, Y. Yang, C. Wun, M. Antman-Passig, H.-B. Luo, S. Cho, K. Long-Roche, L. V. Ramanathan, A. Jagota, M. Zheng, Y. Wang, D. A. Heller, Detection of ovarian cancer via the spectral fingerprinting of quantum-defect-modified carbon nanotubes in serum by machine learning. *Nat. Biomed. Eng.* **6**, 267–275 (2022).
23. M. Kim, C. Chen, Z. Yaari, R. Frederiksen, E. Randall, J. Wollowitz, C. Cupo, X. Wu, J. Shah, D. Worroll, R. E. Lagenbacher, D. Goerzen, Y.-M. Li, H. An, Y. Wang, D. A. Heller, Nanosensor-based monitoring of autophagy-associated lysosomal acidification in vivo. *Nat. Chem. Biol.* **19**, 1448–1457 (2023).
24. X. Wu, M. Kim, L. J. Wang, A. K. Veetil, Y. Wang, Programming sp^3 quantum defects along carbon nanotubes with halogenated DNA. *J. Am. Chem. Soc.* **146**, 8826–8831 (2024).
25. L. R. Powell, Y. Piao, Y. Wang, Optical Excitation of Carbon Nanotubes Drives Localized Diazonium Reactions. *J. Phys. Chem. Lett.* **7**, 3690–3694 (2016).
26. N. F. Zorn, F. J. Berger, J. Zaumseil, Charge Transport in and Electroluminescence from sp3-Functionalized Carbon Nanotube Networks. *ACS Nano* **15**, 10451–10463 (2021).
27. J. L. Bahr, J. Yang, D. V. Kosynkin, M. J. Bronikowski, R. E. Smalley, J. M. Tour, Functionalization of Carbon Nanotubes by Electrochemical Reduction of Aryl Diazonium Salts: A Bucky Paper Electrode. *J. Am. Chem. Soc.* **123**, 6536–6542 (2001).
28. Y. Zheng, S. M. Bachilo, R. B. Weisman, Controlled Patterning of Carbon Nanotube Energy Levels by Covalent DNA Functionalization. *ACS Nano* **13**, 8222–8228 (2019).
29. Y. Zheng, B. M. Weight, A. C. Jones, V. Chandrasekaran, B. J. Gifford, S. Tretiak, S. K. Doorn, H. Htoon, Photoluminescence Dynamics Defined by Exciton Trapping Potential of Coupled Defect States in DNA-Functionalized Carbon Nanotubes. *ACS Nano* **15**, 923–933 (2021).
30. Y. Zheng, Y. Kim, A. C. Jones, G. Olinger, E. R. Bittner, S. M. Bachilo, S. K. Doorn, R. B. Weisman, A. Piryatinski, H. Htoon, Quantum Light Emission from Coupled Defect States in DNA-Functionalized Carbon Nanotubes. *ACS Nano* **15**, 10406–10414 (2021).
31. N. Soltani, R. B. Weisman, Molecular dynamics insights into the guanine functionalization of single-wall carbon nanotubes. *J. Phys. Chem. B* **129**, 6847–6860 (2025).
32. A. A. Alizadehmojarad, S. M. Bachilo, R. B. Weisman, Guanine functionalization of single-wall carbon nanotubes: a quantum chemical study. *ACS Nano* **19**, 21038–21045 (2025).
33. M. Lyu, C. Li, Y. Liu, Y. Li, M. Zheng, A salt-driven mechanism for precise chirality sorting of carbon nanotubes. *Sci. Adv.* **11**, eadx3958 (2025).
34. M. Lyu, B. Meany, J. Yang, Y. Li, M. Zheng, Toward Complete Resolution of DNA/Carbon Nanotube Hybrids by Aqueous Two-Phase Systems. *J. Am. Chem. Soc.* **141**, 20177–20186 (2019).
35. G. Ao, J. K. Streit, J. A. Fagan, M. Zheng, Differentiating Left- and Right-Handed Carbon Nanotubes by DNA. *J. Am. Chem. Soc.* **138**, 16677–16685 (2016).
36. G. Ao, C. Y. Khripin, M. Zheng, DNA-Controlled Partition of Carbon Nanotubes in Polymer Aqueous Two-Phase Systems. *J. Am. Chem. Soc.* **136**, 10383–10392 (2014).
37. M. S. Dresselhaus, G. Dresselhaus, R. Saito, A. Jorio, Raman spectroscopy of carbon nanotubes. *Phys. Rep.* **409**, 47–99 (2005).
38. A. Setaro, M. Adeli, M. Glaeske, D. Przyrembel, T. Bisswanger, G. Gordeev, F. Maschietto, A. Faghani, B. Paulus, M. Weinelt, R. Arenal, R. Haag, S. Reich, Preserving π-conjugation in covalently functionalized carbon nanotubes for optoelectronic applications. *Nat. Commun.* **8**, 14281 (2017).
39. K. Zhang, N. Marzari, Q. Zhang, Covalently Functionalized Metallic Single-Walled Carbon Nanotubes Studied Using Electrostatic Force Microscopy and Dielectric Force Microscopy. *J. Phys. Chem. C* **117**, 24570–24578 (2013).
40. H. Park, J. Zhao, J. P. Lu, Effects of Sidewall Functionalization on Conducting Properties of Single Wall Carbon Nanotubes. *Nano Lett.* **6**, 916–919 (2006).
41. H. L. Zhuang, G. P. Zheng, A. K. Soh, Interactions between transition metals and defective carbon nanotubes. *Comput. Mater. Sci.* **43**, 823–828 (2008).
42. M. Holzinger, J. Abraham, P. Whelan, R. Graupner, L. Ley, F. Hennrich, M. Kappes, A. Hirsch, Functionalization of single-walled carbon nanotubes with (R-)oxycarbonyl nitrenes. *J. Am. Chem. Soc.* **125**, 8566–8580 (2003).
43. C. Liu, Q. Zhang, F. Stellacci, N. Marzari, L. Zheng, Z. Zhan, Carbene-Functionalized Single-Walled Carbon Nanotubes and Their Electrical Properties. *Small* **7**, 1257–1263 (2011).
44. K. Hayashi, Y. Niidome, T. Shiga, B. Yu, Y. Nakagawa, D. Janas, T. Fujigaya, T. Shiraki, Azide modification forming luminescent sp^2 defects on single-walled carbon nanotubes for near-infrared defect photoluminescence. *Chem. Commun.* **58**, 11422–11425 (2022).

45. J. Zhao, H. Park, J. Han, J. P. Lu, Electronic Properties of Carbon Nanotubes with Covalent Sidewall Functionalization. *J. Phys. Chem. B* **108**, 4227–4230 (2004).
46. K. Kamaras, M. E. Itkis, H. Hu, B. Zhao, R. C. Haddon, Covalent Bond Formation to a Carbon Nanotube Metal. *Science* **301**, 1501–1501 (2003).
47. A. H. Brozena, M. Kim, L. R. Powell, Y. Wang, Controlling the optical properties of carbon nanotubes with organic colour-centre quantum defects. *Nat. Rev. Chem.* **3**, 375–392 (2019).
48. F. J. Berger, J. Lüttgens, T. Nowack, T. Kutsch, S. Lindenthal, L. Kistner, C. C. Müller, L. M. Bongartz, V. A. Lumsargis, Y. Zakharko, J. Zaumseil, Brightening of Long, Polymer-Wrapped Carbon Nanotubes by sp3 Functionalization in Organic Solvents. *ACS Nano* **13**, 9259–9269 (2019).
49. X. He, I. Kevlishvili, K. Murcek, P. Liu, A. Star, [2π + 2π] photocycloaddition of enones to single-walled carbon nanotubes creates fluorescent quantum defects. *ACS Nano* **15**, 4833–4844 (2021).
50. H. Qu, Y. Han, J. Fortner, X. Wu, S. Kilina, D. Kilin, S. Tretiak, Y. Wang, [2 + 2] Cycloaddition Produces Divalent Organic Color-Centers with Reduced Heterogeneity in Single-Walled Carbon Nanotubes. *J. Am. Chem. Soc.* **146**, 23582–23590 (2024).
51. Y. Zheng, S. M. Bachilo, R. B. Weisman, Photoexcited Aromatic Reactants Give Multicolor Carbon Nanotube Fluorescence from Quantum Defects. *ACS Nano* **14**, 715–723 (2020).
52. J. Chen, Y. Li, J. Wu, J. Liu, X. Zhou, Z. Li, K. Tang, L. Shi, Z. Zhang, Z. Lin, Ordered DNA-Wrapped Single-Chirality Carbon Nanotubes Enable an Unparalleled Sensing Platform for Copper Ion Detection. *ACS Nano* **19**, 28743–28754 (2025).
53. M. E. Sykes, M. Kim, X. Wu, G. P. Wiederrecht, L. Peng, Y. Wang, D. J. Gosztola, X. Ma, Ultrafast Exciton Trapping at sp3 Quantum Defects in Carbon Nanotubes. *ACS Nano* **13**, 13264–13270 (2019).
54. T. Eremin, R. Dhama, H. Caglayan, P. Obraztsov, Ultrafast exciton trapping dynamics in oxygen-functionalized single-walled carbon nanotubes. *Carbon* **220**, 118837 (2024).
55. R. Berera, R. van Grondelle, J. T. M. Kennis, Ultrafast transient absorption spectroscopy: principles and application to photosynthetic systems. *Photosynth. Res.* **101**, 105–118 (2009).
56. M. Liu, O. Voznyy, R. Sabatini, F. P. García de Arquer, R. Munir, A. H. Balawi, X. Lan, F. Fan, G. Walters, A. R. Kirmani, S. Hoogland, F. Laquai, A. Amassian, E. H. Sargent, Hybrid organic–inorganic inks flatten the energy landscape in colloidal quantum dot solids. *Nat. Mater.* **16**, 258–263 (2017).
57. N. Droseros, P. Ferdowsi, E. O. Martinez, M. Saliba, N. Banerji, D. Tsokkou, Excited-State Dynamics of MAPbBr3: Coexistence of Excitons and Free Charge Carriers at Ultrafast Times. *J. Phys. Chem. C* **128**, 8637–8648 (2024).
58. M. Kim, X. Wu, G. Ao, X. He, H. Kwon, N. F. Hartmann, M. Zheng, S. K. Doorn, Y. Wang, Mapping Structure-Property Relationships of Organic Color Centers. *Chem* **4**, 2180–2191 (2018).
59. R. R. Johnson, A. T. C. Johnson, M. L. Klein, Probing the Structure of DNA−Carbon Nanotube Hybrids with Molecular Dynamics. *Nano Lett.* **8**, 69–75 (2008).
60. S. Meng, P. Maragakis, C. Papaloukas, E. Kaxiras, DNA Nucleoside Interaction and Identification with Carbon Nanotubes. *Nano Lett.* **7**, 45–50 (2007).
61. X. Fang, H. Ren, M. Gu, Orbital angular momentum holography for high-security encryption. *Nat. Photonics* **14**, 102–108 (2020).
62. J. Bai, Z. Shi, X. Jiang, "Acrostic" Encryption: Stress-Manipulation on Information Display. *Adv. Funct. Mater.* **33**, 2301797 (2023).
63. P. Chen, D. Li, Z. Li, L. Pi, X. Xu, H. Wang, X. Zhou, T. Zhai, Electric-Tunable Photoluminescence of 2D ErOCl for High-Security Encryption of Programmable Information. *Adv. Opt. Mater.* **10**, 2102562 (2022).
64. C. Zhang, B. Wang, W. Li, S. Huang, L. Kong, Z. Li, L. Li, Conversion of invisible metal-organic frameworks to luminescent perovskite nanocrystals for confidential information encryption and decryption. *Nat. Commun.* **8**, 1138 (2017).
65. J. Wang, J. Ma, J. Zhang, Y. Fan, W. Wang, J. Sang, Z. Ma, H. Li, Advanced Dynamic Photoluminescent Material for Dynamic Anticounterfeiting and Encryption. *ACS Appl. Mater. Interfaces* **11**, 35871–35878 (2019).
66. M. Pan, C. Wang, Y. Hu, X. Wang, L. Pan, Y. Lin, L. Shang, H. Xu, J. Zhao, Y. Li, Dual Optical Information-Encrypted/Decrypted Invisible Photonic Patterns based on Controlled Wettability. *Adv. Opt. Mater.* **10**, 2101268 (2022).
67. J.-Q. Zhao, H.-S. Shi, L.-R. Zeng, H. Ge, Y.-H. Hou, X.-M. Wu, C.-Y. Yue, X.-W. Lei, Highly emissive zero-dimensional antimony halide for anti-counterfeiting and confidential information encryption-decryption. *Chem. Eng. J.* **431**, 134336 (2022).
68. Y. Li, Z. Lin, https://www.notion.so/InfoEncrypt-Compiler-Download-934 32b79e4de5be807fa948f19351a6ab7f?source=copy_link *InfoEncrypt Compiler*.
69. D. Goerzen, M. Kim, C. Schroff, M. N. Hoang, J. S. Wollowitz, A. Kolb, J. P. Walshon, K. McCortney, C. Horbinski, K. Galbraith, S. Raoof, M. Snuderl, A. Ordureau, D. A. Heller, Machine perception liquid biopsy identifies brain tumours via systemic immune and tumour microenvironment signature. *Nat. Nanotechnol.* **21**, 277–287 (2026).
70. M. Zheng, Structure-Defined DNA-Carbon Nanotube Hybrids and Their Applications. *ECS Trans.* **85**, 511–517 (2018).
71. Y. Li, Y. Wen, L. C. Beltrán, L. Zhu, S. Tian, J. Liu, X. Zhou, P. Chen, E. H. Egelman, M. Zheng, Z. Lin, Understanding DNA-encoded carbon nanotube sorting and sensing via sub-nm-resolution structural determination. *Sci Adv.* **11**, eadt9844 (2025).
72. F. Neese, Software update: the ORCA program system—version 5.0. *WIREs Comput. Mol. Sci.* **12**, e1606 (2022).
73. J. P. Perdew, K. Burke, M. Ernzerhof, Generalized gradient approximation made simple. *Phys. Rev. Lett.* **77**, 3865–3868 (1996).
74. F. Weigend, R. Ahlrichs, Balanced basis sets of split valence, triple zeta valence and quadruple zeta valence quality for H to Rn: design and assessment of accuracy. *Phys. Chem. Chem. Phys.* **7**, 3297–3305 (2005).

Acknowledgments

Funding: Z.L. acknowledges supports from the National Key Research and Development Program of China (No. 2023YFA0915200), the National Natural Science Foundation of China (NSFC No. 52273265, 52573294), the Guangdong Basic and Applied Basic Research Foundation (No. 2024A1515012437, 2024B1515040023), the R&D Program of Guangzhou (No. 2025A04J7015), the GJYC program of Guangzhou (No. 2024D03J0002, 2024D01J0057), the Fundamental Research Funds for the Central Universities (2025ZYGXZR052), State Key Lab of Luminescent Materials and Devices, South China University of Technology (Skllmd-2026-05), and the Xiaomi Foundation. C.-Q.X. acknowledges Shenzhen Science and Technology Program (grant no. RCYX20231211090357078). Z.Z. acknowledges supports from the National Natural Science Foundation of China (12474031, W2433157), the Guangdong Basic and Applied Basic Research Foundation (2025A1515010298), the Pearl River Talent Program of Guangdong Province (2023QN10C450s), and the GJYC program of Guangzhou (2024D01J0078, 2024D03J0007). **Author contributions:** Conceptualization: Y.L., Z.Z., and Z.L. Methodology: Y.L., X.Z., Z.Z., C.-Q.X., and Z.L. Software: Z.L. Validation: Y.L., X.Z., J.W., L.Z., Y.F., Z.Z. C.-Q.X, and Z.L. Formal analysis: Y.L., X.Z., J.W., L.Z., C.-Q.X. and Z.L. Investigation: Y.L., X.Z., J.W., Z.Z., and Z.L. Resources: Y.L., X.Z., J.W., S.T., Y.F., Z.Z., C.-Q.X., and Z.L. Data curation: Y.L., X.Z., J.W., L.Z., S.T., and Z.L. Writing–original draft: Y.L. and Z.L. Writing—review and editing: Y.L., X.Z., C.-Q.X., and Z.L. Visualization: Y.L., X.Z., J.W, C.-Q.X., and Z.L. Supervision: Z.Z. and Z.L. Project administration: Z.L. Funding acquisition: Z.Z., C.-Q.X., and Z.L. **Competing interests:** The authors declare no competing interests. **Data, code, and materials availability:** All data and code needed to evaluate and reproduce the results in the paper are present in the paper and/or the Supplementary Materials. This study did not generate new materials. The procedure for single-chirality CNTs is described in the "Purification of single-chirality CNTs" section of the Materials and Methods. The procedure for guanine-functionalized CNTs is described in the "CNT functionalization by guanine chemistry" section of the Materials and Methods. All ssDNA oligomers utilized for CNT separation and functionalization were purchased from Sangon Biotech. The sequences are listed in table S1 and figs. S7, S24H, and S27.

Submitted 18 December 2025
Accepted 28 May 2026
Published 10 July 2026
10.1126/sciadv.aee8922

ScienceAdvances

Inverse design of guanine-defects in carbon nanotubes for high-resolution emission tuning

Yinong Li, Xiao-Kun Zhao, Jiajie Wu, Li Zhu, Shishan Tian, Yannan Feng, Zhilong Zhang, Cong-Qiao Xu, and Zhiwei Lin

Sci. Adv. **12** (28), eaee8922. DOI: 10.1126/sciadv.aee8922

Science Advances (ISSN 2375-2548) is published by the American Association for the Advancement of Science. 1200 New York Avenue NW, Washington, DC 20005. The title *Science Advances* is a registered trademark of AAAS.